Stabilizing the metastable superhard material wurtzite boron nitride by three-dimensional networks of planar defects

Chunlin Chen[a,b,1], Deqiang Yin[b,c], Takeharu Kato[d], Takashi Taniguchi[e], Kenji Watanabe[e], Xiuliang Ma[a,1], Hengqiang Ye[a], and Yuichi Ikuhara[b,d,f,1]

[a]Shenyang National Laboratory for Materials Science, Institute of Metal Research, Chinese Academy of Sciences, 110016 Shenyang, China; [b]Advanced Institute for Materials Research, Tohoku University, 980-8577 Sendai, Japan; [c]College of Aerospace Engineering, Chongqing University, 400044 Chongqing, China; [d]Nanostructures Research Laboratory, Japan Fine Ceramics Center, 456-8587 Nagoya, Japan; [e]National Institute for Materials Science, Tsukuba, 305-0044 Ibaraki, Japan; and [f]Institute of Engineering Innovation, The University of Tokyo, 113-8656 Tokyo, Japan

Wurtzite boron nitride (w-BN) is a metastable superhard material that is a high-pressure polymorph of BN. Clarifying how the metastable high-pressure material can be stabilized at atmospheric pressure is a challenging issue of fundamental scientific importance and promising technological value. Here, we fabricate millimeter-size w-BN bulk crystals via the hexagonal-to-wurtzite phase transformation at high pressure and high temperature. By combining transmission electron microscopy and ab initio molecular dynamics simulations, we reveal a stabilization mechanism for w-BN, i.e., the metastable high-pressure phase can be stabilized by 3D networks of planar defects which are constructed by a high density of intersecting (0001) stacking faults and {10$\bar{1}$0} inversion domain boundaries. The 3D networks of planar defects segment the w-BN bulk crystal into numerous nanometer-size prismatic domains with the reverse crystallographic polarities. Our findings unambiguously demonstrate the retarding effect of crystal defects on the phase transformations of metastable materials, which is in contrast to the common knowledge that the crystal defects in materials will facilitate the occurrence of phase transformations.

metastable phase | superhard material | planar defect | electron microscopy

Wurtzite boron nitride (w-BN) has attracted intense interest due to its outstanding properties and potential applications. w-BN is a fascinating superhard material with a hardness next to diamond (1–3), rendering it a candidate material to replace diamond. w-BN is also a promising III-V group wide-bandgap material for advanced electronic devices because it has many properties superior to GaN and AlN, such as a wider band gap, higher thermal conductivity, and larger spontaneous polarization (4, 5). Since the first synthesis of w-BN in the 1960s (6), extensive efforts have been devoted to the fabrication of high-quality w-BN samples (7–11), the in-depth understanding of phase transformations between BN polymorphs (12–16), and the theoretical investigation of deformation mechanisms of w-BN (17). Unfortunately, such efforts are greatly hampered by the technical difficulties in stabilizing w-BN at atmospheric pressure. The w-BN phase obtained by the direct conversion of hexagonal BN (h-BN) at high pressure tends to recover to the h-BN phase after releasing pressure, and only a small amount of w-BN can maintain its structure (12, 15, 18, 19). The prevailing synthesis method of w-BN is the shock compression of h-BN, which can only produce w-BN fine powders with micrometer grain size, and other BN impurities are readily introduced (7, 13, 20, 21). Synthesis of w-BN bulk crystals is challenging due to lack of efficient approaches for stabilizing the metastable high-pressure phase. Since w-BN is a thermodynamically metastable phase, w-BN single crystals cannot be fabricated by a dissolution and precipitation process. When BN crystals were recrystallized by solvent system, only h-BN or cubic BN (c-BN) crystals were grown

at their stable pressure and temperature condition. Similar features were known in carbon system as a hexagonal diamond (h-diamond). However, w-BN can be partially quenchable after transformed from h-BN, while h-diamond will almost totally transform back into graphite. This known feature has so far never been reasonably explained.

For stabilizing metastable high-temperature phases, element doping is an efficient way. For example, the addition of Y_2O_3 can stabilize cubic ZrO_2 at room temperature, though it is a metastable phase existing above 2,690 °C (22). However, this method should be ineffective for stabilizing w-BN since the solubility of dopants in w-BN is quite low owing to the very strong sp^3 bonding. The stabilization of metastable high-pressure phases such as w-BN and its analog in carbon system—lonsdaleite (i.e., h-diamond)—remains to be extremely challenging because of the very low kinetic barrier for the transformation back to ambient phases (23, 24). Thus, finding new mechanisms for stabilizing the metastable high-pressure phases at ambient pressure is of both fundamental academic interest and technological significance.

Effects of crystal defects on phase transformations have been studied for over a century. Since crystal defects have higher energy than the perfect region, they usually serve as nucleation sites for the phase transformations (25). In addition, crystal defects can also act as sinks or diffusion channels for dopants and

Significance

Metastable high-pressure materials often possess outstanding properties. However, the stabilization of metastable high-pressure materials usually is challenging due to the very low kinetic barrier for the transformation back to ambient phases. Wurtzite boron nitride (w-BN) is a metastable high-pressure polymorph of BN, which can only be fabricated as micrometer-size powders by the shock compression of hexagonal BN. Here, we fabricate millimeter-size w-BN bulk crystals and reveal an unprecedented stabilization mechanism for w-BN. We find that the metastable high-pressure phase can be stabilized by 3D networks of planar defects. Our findings unambiguously demonstrate the retarding effect of crystal defects on the phase transformations of metastable materials.

ENGINEERING

promote the occurrence of diffusional phase transformations (25). In contrast to the well-known promoting role, the retarding effect of crystal defects on phase transformations still remains unexplored.

Here, we convert millimeter-size h-BN bulk crystals to the w-BN phase at 10 GPa and 850 °C, and stabilize the w-BN bulk crystals to the ambient pressure and temperature. The stabilization mechanism of w-BN is investigated by transmission electron microscopy (TEM) and ab initio molecular dynamics (MD) simulations.

Fig. 1A shows a photograph of a high-purity h-BN single crystal synthesized at 4.5 GPa and 1,500 °C using barium BN as a solvent (26). The transparent h-BN single crystal has a shape of hexagonal prism with diameter of ~1 mm and thickness of ~0.5 mm. For the synthesis of w-BN, the h-BN crystal has been used as the source material and annealed at 10 GPa and 850 °C for 20 min and then quenched to room temperature and atmospheric pressure (more synthesis details are shown in *SI Appendix*, Fig. S1). The crystal after high pressure and high temperature treatment is shown in Fig. 1B. Clearly, the crystal retains the shape of hexagonal prism and the diameter of ~1 mm, while it changes to a black color and its thickness reduces by ~40% to ~0.3 mm, indicating the occurrence of phase transformations. X-ray diffraction (XRD) patterns of the crystal before and after phase transformation are shown in Fig. 1C, which can be consistently indexed as those of h-BN and w-BN without additional visible peaks of other impurities. The 2Θ angle of the w-BN (0002) diffraction is 43.04°. The h-BN and w-BN crystal have been crushed into powders to measure their powder XRD patterns (*SI Appendix*, Fig. S2), which confirm again that the initial transparent crystal and the as-synthesized black crystal are composed of the h-BN [instead of the rhombohedral BN phase (27)] and w-BN phases, respectively. The Raman spectrum taken from the black w-BN crystal is shown in

Fig. 1D. The Raman peaks match well with the E_2, $E_1(TO)$, and $E_1(LO)$ peaks of w-BN predicted by first-principles calculations (28). Further experiments reveal that the h-BN crystal will be transformed into c-BN if annealed at 10 GPa and 1,200 °C. The measured 2Θ angle of the c-BN (111) diffraction is 43.34° [i.e., 0.3° larger than that of the w-BN (0002) diffraction]. The powder XRD pattern obtained from the crushed powder of c-BN crystals is shown in *SI Appendix*, Fig. S2C, which is evidently different from that of w-BN.

To reveal the structural features for the unusual stability of the w-BN bulk crystal, TEM characterizations were carried out. Fig. 2 presents bright-field TEM images and selected-area electron diffraction (SAED) patterns of the w-BN crystal from two orthogonal directions. As shown in Fig. 2A, the w-BN bulk crystal is polycrystalline and has a textured structure with all grains highly oriented. Two sets of perpendicular and intersecting planar defects are formed in nearly all grains. The average interval of each set is less than 15 nm, indicating that the density of planar defects in the w-BN bulk crystal is extremely high compared with the c-BN bulk crystal prepared at high temperature and high pressure conditions (29). Fig. 2B shows the corresponding SAED pattern, which unambiguously reveals that the two sets of planar defects are formed on the (0001) basal and ($01\bar{1}0$) prismatic planes, respectively. The planar defects on the (0001) plane should be intrinsic stacking faults (ISFs), and those on the ($01\bar{1}0$) plane should be inversion domain boundaries (IDBs) (30, 31). Fig. 2 C and D show the bright-field TEM image and corresponding SAED pattern obtained from the orthogonal [$0\bar{1}10$] zone axis, respectively. Obviously, no planar defect can be seen in this TEM image, indicating that there are no planar defects on the ($\bar{2}110$) plane. The (0001) stacking faults become invisible since their displacement vectors cannot be identified from this projection.
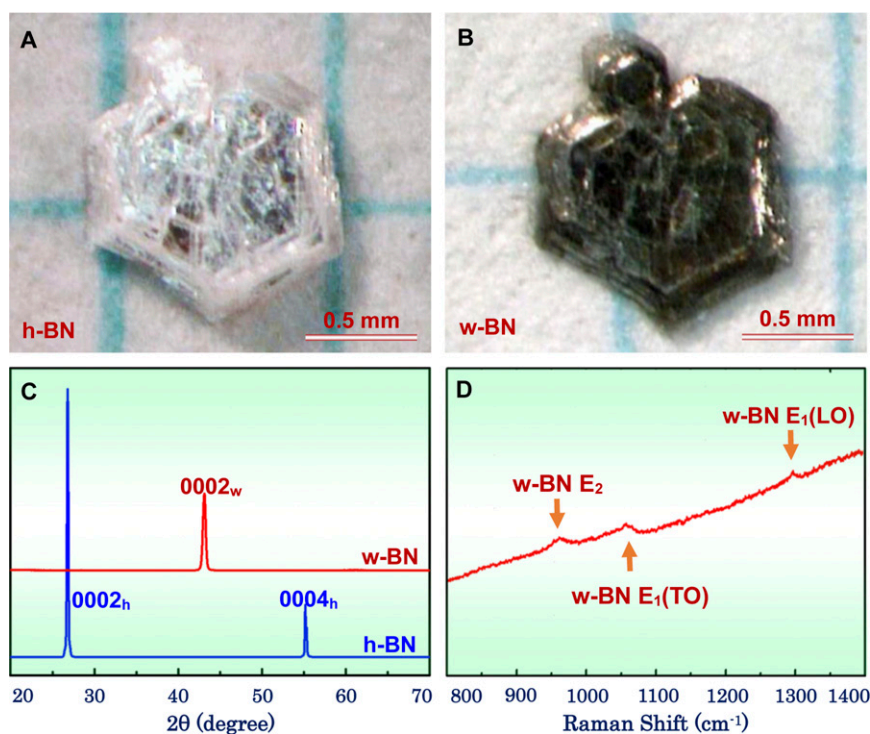
Fig. 1. Synthesis of w-BN bulk crystals via the direct conversion of h-BN crystals at high pressure and high temperature. (A) Photograph of the high-purity h-BN bulk crystal. (B) As-synthesized w-BN bulk crystal appearing a black color. (C) XRD patterns of the crystal before and after the phase transformation. (D) Raman spectrum comprising the E_2, $E_1(TO)$, and $E_1(LO)$ peaks taken from the black w-BN crystal.

Chen et al.
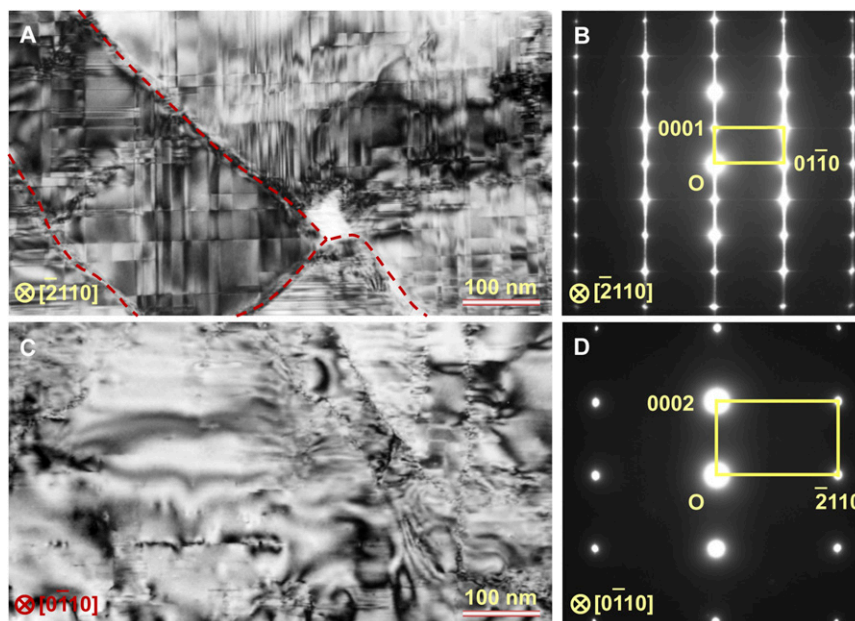
Fig. 2. Microstructure of the w-BN crystal viewing from two orthogonal projections. (*A* and *B*) Bright-field TEM image (*A*) and SAED pattern recorded along the [$\bar{2}$110] direction (*B*). Two sets of planar defects (i.e., ISF and IDB) are formed on the (0001) basal and (01$\bar{1}$0) prismatic planes, respectively. The dashed red lines indicate the grain boundaries. (*C* and *D*) Bright-field TEM image (*C*) and SAED pattern viewed from the [0$\bar{1}$10] direction (*D*). There are no planar defects on the ($\bar{2}$110) plane.

To reveal atomic details, we performed spherical aberration-corrected scanning TEM (STEM) imaging of the (0001) ISFs and (01$\bar{1}$0) IDBs from the [$\bar{2}$110] projection using both high-angle annular dark field (HAADF) and annular bright-field (ABF) techniques. Fig. 3 *A* and *B* show the simultaneously recorded HAADF and ABF STEM images of the (0001) ISF. Since the atomic columns with heavier elements have stronger intensities in the HAADF images (32), we can conveniently distinguish nitrogen (N) and boron (B) atomic columns in BNs through comparison of the intensities of atomic columns (29). On the other hand, the ABF STEM technique is more powerful for imaging light elements than the HAADF (33). Both the HAADF and ABF images reveal that the (0001) ISF modifies the stacking sequence of atomic layers in w-BN from the hexagonal ABAB... type to the face-centered cubic (FCC) ABC... type (as denoted by the inserted atomic model), rendering the atomic structure of the ISF equivalent to that of three layers of c-BN which has the FCC-type ABCABC... stacking sequence. The (0001) ISF does not invert the crystallographic polarity of w-BN. Fig. 3 *C* and *D* show the HAADF and ABF STEM images of the (01$\bar{1}$0) IDB. The most important structural characteristic of the IDB is that it reverses the crystallographic polarity of w-BN. The N sublattice locates above the B sublattice on the left side of the IDB, while on the right side, the N sublattice sits below the B sublattice. Fig. 3 *E* and *F* are the HAADF and ABF STEM images presenting the intersection of the (0001) ISF and (01$\bar{1}$0) IDB. The two orthogonal planar defects penetrate each other and construct an ISF–IDB junction. The ISF structural units adopt a mirror orientation with respect to the IDB plane, which induces the formation of a mixed-type partial dislocation $\mathbf{b} = 1/3[10\bar{1}0]$. A schematic atomic configuration of the ISF–IDB junction is shown in *SI Appendix*, Fig. S3, which was proved to have a low formation energy via empirical potential calculations based on the GaN models (34).

By combining the structural information conveyed by Figs. 2 and 3, we draw a schematic diagram (Fig. 4) that represents unambiguously the 3D configurations of the (0001) ISFs and {10$\bar{1}$0} IDBs in the w-BN crystal and the crystallographic polarities of the numerous nanometer-size prismatic domains enclosed by these planar defects. Since w-BN has a hexagonal structure which has three equivalent (01$\bar{1}$0), (10$\bar{1}$0), and (1$\bar{1}$00) crystal planes, the formation ratios of IDBs on these three planes are equal. Therefore, the w-BN bulk crystal must comprise simultaneously the (01$\bar{1}$0), (10$\bar{1}$0), and (1$\bar{1}$00) IDBs (denoted by IDB$_{m1}$, IDB$_{m2}$, and IDB$_{m3}$). The 3D networks of planar defects segment the w-BN bulk crystal into numerous prismatic domains with sizes of tens of nanometers. Since the {01$\bar{1}$0} IDBs will invert the crystallographic polarity of w-BN, the adjacent domains beside the {10$\bar{1}$0} IDBs have the reverse crystallographic polarities (denoted by green and yellow colors in Fig. 4). The (0001) ISFs will not change the crystallographic polarity of w-BN domains. The 3D networks of planar defects could, in principle, retard the w-BN to h-BN phase transformation and stabilize the metastable w-BN phase due to the following reasons. First, the (0001) ISFs of w-BN actually have the same atomic structure as three layers of c-BN (Fig. 3 *A* and *B*), which is more stable than w-BN and will not recover to h-BN after releasing pressure. Second, the 3D networks of planar defects segment the w-BN bulk crystal into numerous nanometer-size domains. It was found that the nanometer-scale grain size could benefit significantly for stabilizing high-pressure phases of TiO$_2$ due to the energy barrier for nucleation of low-pressure polymorphs (35, 36). The nanometer-scale domain size of w-BN may suppress the nucleation of h-BN and stabilize the w-BN via a similar mechanism. Third, the intersections of the (0001) ISFs and {10$\bar{1}$0} IDBs lead to the formation of numerous ISF–IDB junctions whose junction line defects are mixed-type partial dislocations $\mathbf{b} = 1/3\langle 10\bar{1}0\rangle$. Since the w-BN to h-BN phase transformation will cause a lattice expansion of ∼40% along the c axis, the nucleation of h-BN from the w-BN matrix needs the movement of the ISF–IDB junctions along the [0001] direction. While the slip planes of the $\mathbf{b} = 1/3\langle 10\bar{1}0\rangle$ mixed-type partial dislocations are the basal (0001) planes, it is extremely difficult to move the ISF–IDB junctions along the c axis. As a result, the numerous ISF–IDB junctions in w-BN will suppress the nucleation of h-BN.

To reveal the stabilizing effect of the stacking faults on BN phase transformations, we have qualitatively compared the
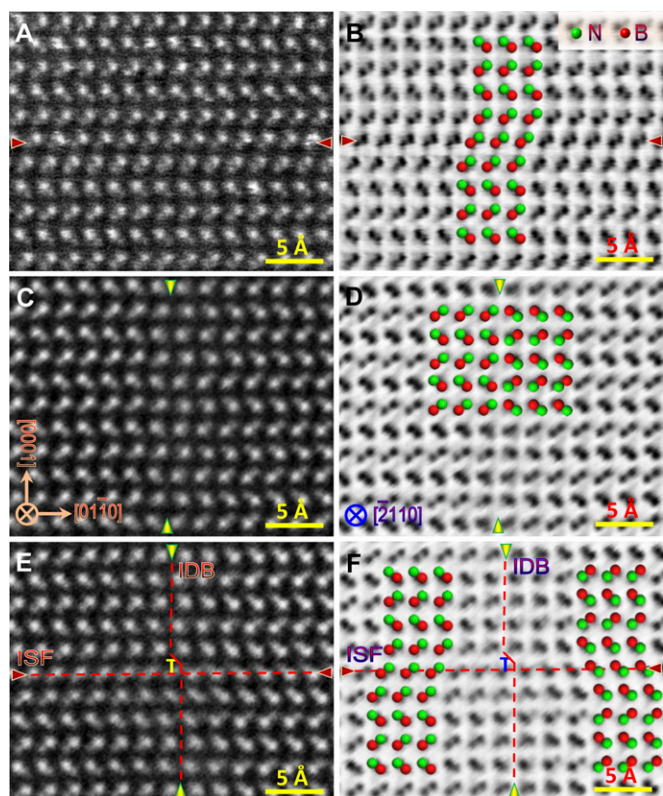
Fig. 3. Identifying atomic-scale structure of the ISF and IDB in w-BN along the [$\bar{2}$110] zone axis. (*A* and *B*) HAADF and ABF STEM images showing the atomic structure of the (0001) ISF. The (0001) ISF only modifies the stacking sequence of w-BN. (*C* and *D*) HAADF and ABF STEM images showing the atomic structure of the (01$\bar{1}$0) IDB. The (01$\bar{1}$0) IDB inverts the crystallographic polarity of w-BN. (*E* and *F*) HAADF and ABF STEM images showing the intersection of the (0001) ISF and (01$\bar{1}$0) IDB. The two orthogonal planar defects penetrate each other and construct an ISF–IDB junction, inducing the formation of a mixed-type partial dislocation **b** = 1/3[10$\bar{1}$0]. The ISFs and IDBs are indicated by the red and yellow arrowheads, respectively.

thermal stability of w-BN with and without the (0001) ISF by ab initio MD simulations (due to lack of B–N potentials applicable for both sp^3-bonded w-BN and sp^2-bonded h-BN, it is difficult to mimic the w-BN to h-BN phase transformation by classical MD simulations). The phase transformation process of the perfect w-BN and that with one (0001) ISF are shown in Fig. 5 *A–D* and *E–H*, respectively. The initial candidate models are fully relaxed by fixing the bottom atomic layer and adding the vacuum region of 20 Å on the top to construct the surface configurations. After optimization at 0 K, both structures remain stable, except the surface reconstruction of the top layer due to the surface effect (Fig. 5 *A* and *E*). With the increase of temperature, the phase transformation from w-BN to an h-BN–like structure occurs initially from the surface and gradually propagates to the inner for both cases. The sp^3 bonds in the w-BN convert to the sp^2 bonds after the phase transformation. For the perfect w-BN, three layers of w-BN are transformed to the h-BN–like structure at 50 K (Fig. 5*B*), and four layers at 64 K (Fig. 5*C*). When temperature reaches 97 K, the w-BN phase is completely transformed to the h-BN–like structure (Fig. 5*D*). By introducing one (0001) ISF into the w-BN, the phase transformation has been retarded significantly. As shown in Fig. 5 *F* and *G*, the phase transformation of three and four layers of w-BN requires the increase of temperature to 170 K and 200 K, respectively. The complete phase transformation is finished at 360 K (Fig. 5*H*), which is 263 K higher than the case of perfect w-BN.

Finally, it is best to clarify the implications of this study from the viewpoints of materials science and geoscience. In general, fabricating w-BN bulk crystals and revealing the stabilization mechanism can significantly contribute to materials science in the following aspects. First, this study has unambiguously demonstrated that the 3D networks of planar defects can stabilize the w-BN to the atmospheric pressure via retarding the w-BN to h-BN phase transformation. This finding is in contrast to the common knowledge that the crystal defects in materials will facilitate the occurrence of phase transformations, contributing significantly to phase transformation theory. Second, the stabilization mechanism associated with the retarding effect of crystal defects on the phase transformations should, in principle, be applicable for other metastable materials with low defect-formation energy, shedding light on the innovation of advanced materials under extreme conditions. An important known fact so-far argued is that w-BN crystals can be quenchable after transformed from h-BN, while h-diamond is transformed back into graphite. This study determined the uniqueness of w-BN's defect network mechanism for the stabilization of metastable forms. The 3D networks of planar defects are considered to be a typical feature of the binary system of boron and nitride. In the case of h-diamond of the monoatomic system of carbon, the mechanism of defect network may be totally different, and then back transformation could easily take place. This feature could give rise to inspiration for future work on the stabilization of h-diamond by doping some elements such as boron and nitrogen for stabilizing the defect network found in w-BN. Third, since w-BN has many advantages compared with the widely used electronic materials GaN and AlN, the fabrication of millimeter-size w-BN bulk crystals will encourage the efforts to develop high-performance electronic devices superior to those based on GaN and AlN.

In addition, revealing the stabilization mechanism of w-BN must also contribute potentially to geoscience. Since boron is dominantly distributed at Earth's surface rather than the primitive mantle, boron-containing minerals are ideal tracers for understanding the recycling of crustal material back to the Earth's mantle (37). Natural c-BN (i.e., qingsongite) is the first reported boron mineral from the Earth's mantle, which has been thought not to form naturally in Earth for a long time (38). The discovery
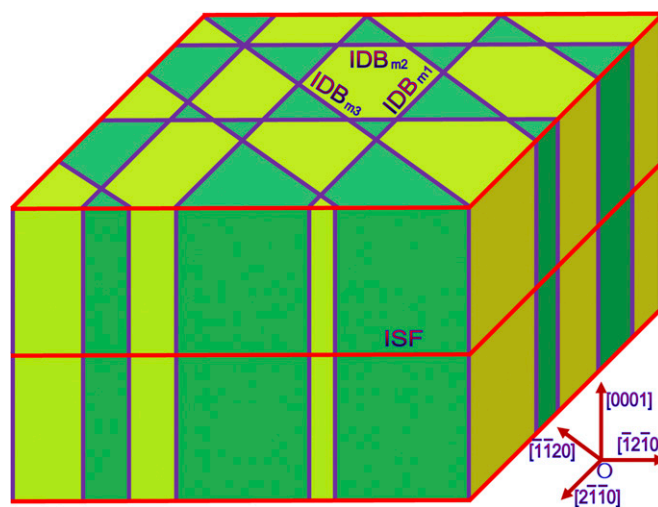
Fig. 4. Schematic diagram representing the 3D configuration of the intersecting (0001) ISFs (red) and {10$\bar{1}$0} IDBs (purple) in the w-BN crystal. The w-BN crystal comprises simultaneously the (01$\bar{1}$0), (10$\bar{1}$0), and (1$\bar{1}$00) IDBs, as indicted by IDB$_{m1}$, IDB$_{m2}$, and IDB$_{m3}$, respectively. The 3D networks of planar defects segment the w-BN bulk crystal into numerous nanometer-size prismatic domains with the reverse crystallographic polarities (denoted by green and yellow colors).

Chen et al.
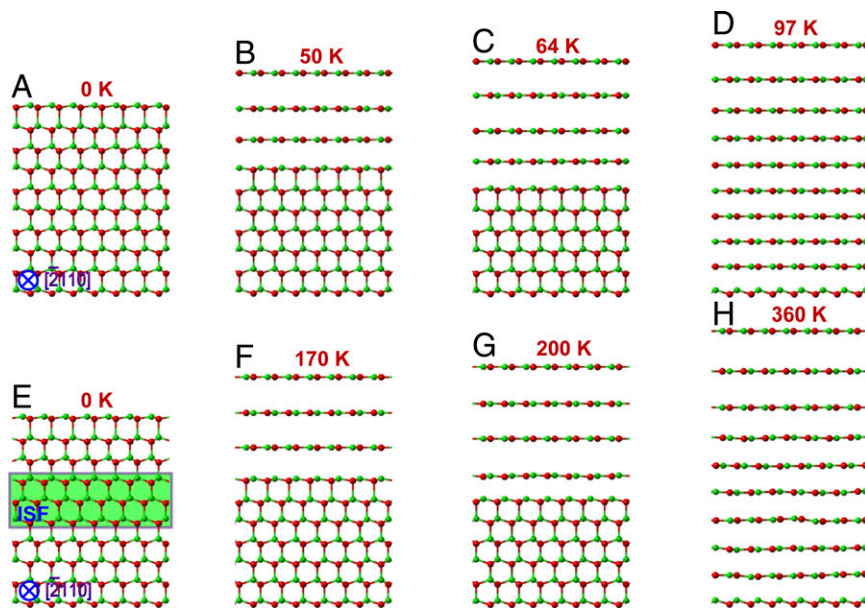
Fig. 5. Comparison of the thermal stability of w-BN with and without the (0001) ISF by ab initio MD simulations. (*A–D*) MD snapshots showing the structural evolution of the perfect w-BN. The w-BN phase gradually transforms to the h-BN–like structure with the increase of temperature to 97 K. (*E–H*) Phase transformation of the w-BN with one (0001) ISF. By introducing one (0001) ISF into the w-BN, the phase transformation has been retarded significantly. The complete phase transformation is finished at 360 K, which is 263 K higher than the case of perfect w-BN.

of qingsongite in 2013 has significantly deepened our understanding of the process and depths of the formation of chromitites in the mantle sections of ophiolites, encouraging us to search for other new high-pressure boron-bearing minerals in the mantle environments (38). Natural w-BN is a potential candidate mineral indicative of deep subduction of crustal material, which can be used as the tracer for the high-pressure geophysical process at a relatively lower temperature compared with the c-BN.

Unveiling the stabilization mechanism of metastable high-pressure materials deepens our understanding of phase transformations under critical conditions. We demonstrate that the metastable high-pressure w-BN phase could be stabilized at atmospheric pressure by 3D networks of planar defects comprising a high density of intersecting ISFs and IDBs. The 3D networks of planar defects segment the w-BN bulk crystal into numerous nanometer-size prismatic domains with the reverse crystallographic polarities. This stabilization mechanism associated with the retarding effect of crystal defects on the phase transformations should, in principle, be applicable for other metastable materials with low defect-formation energy.

Materials and Methods

Sample Preparation and Microscopic Observations. Man-made high-quality h-BN bulk crystals, grown at 4.5 GPa and 1,500 °C by the temperature gradient method (26), were used as the source materials for the fabrication of w-BN bulk crystals. The as-prepared h-BN crystals were then compressed at a uniaxial pressure of 10 GPa along the c axis and annealed for 20 min at 850 °C using a belt-type high-pressure apparatus, and the h-BN was directly converted to the w-BN. After the hexagonal-to-wurtzite phase transformation, the w-BN crystals were quenched to room temperature in 10 s. Finally, the pressure of 10 GPa was released to atmospheric pressure in 90 min. Thin-foil specimens for TEM and STEM imaging were prepared by a focused ion-beam (FIB) technique using a Hitachi NB5000 FIB system, followed by Ar ion-beam thinning to remove the FIB damages. Conventional TEM observations were performed using a JEM-2010F (JEOL Co., Ltd.) microscope. HAADF and ABF imaging were carried out on a 200-kV STEM instrument (ARM200FC; JEOL) using a probe size of ~1 Å, a probe convergence angle of ~25 mrad, and HAADF and ABF collection semiangles for 68 to 280 mrad and 12 to 24 mrad, respectively. STEM image simulations were conducted using the WinHREM package (HREM Research, Inc.) which is coded according to the multislice method (39). The parameters adopted for image simulations are the same as the experimental ones. The atomic models of (0001)

ISFs and {10$\bar{1}$0} IDBs (*SI Appendix*, Fig. S4) for STEM image simulations were obtained by first-principles calculations. The simulated HAADF and ABF images are shown in *SI Appendix*, Fig. S5, which are in excellent agreement with the experimental ones (Fig. 2). The slice thickness and sample thickness for the simulations in *SI Appendix*, Fig. S5 were adopted as 1.27 Å and 7.6 nm, respectively.

Density Functional Theory Calculations. All computations were carried out by the density functional theory (DFT) method using the Vienna Ab Initio Simulation Package (40, 41). The projector augmented wave method (42) was used to describe the electron–ion interaction, with the valence electron on elemental boron and nitrogen in a configuration of $2s^2p^1$ and $2s^2p^3$, respectively. The generalized gradient approximation in Perdew et al. (43) (PW91) was chosen as the exchange-correlation interaction functional. Single-particle Kohn–Sham wave function was expanded using plane wave with a cutoff energy of 400 eV. The irreducible Brillouin zone was sampled with a regular Monkhorst–Pack grid (44) of $3 \times 9 \times 1$ k points for the supercell including the (0001) stacking faults, and $3 \times 15 \times 7$ k points for the supercell including the {10$\bar{1}$0} IDBs (*SI Appendix*, Fig. S4). During the structural optimization, all of the atoms and the sizes of supercells were fully relaxed until the energy tolerance was less than 10^{-4} eV or the magnitude of the Hellmann–Feynman force on each atom converged to less than 0.03 eV/Å. Based on the atomic models obtained by DFT calculations, standard ab initio MD simulations with the constant volume and a continuous increase or decrease of the kinetic energy, where in the intermediate period a microcanonical ensemble was simulated, were performed at DFT level to clarify the stabilizing effect of the ISFs. To mimic the initiation of phase transformation from the surface, a vacuum region of 20 Å was embedded into the boundary to construct the surface configuration, and the bottom layer of atoms was fixed. The k points of $3 \times 7 \times 1$ were adopted with consideration of computational efficiency and accuracy.

We used the following equation to calculate the formation energy, E_f, of the planar defects:

$$E_f = \frac{E_{Supercell} - E_{Perfect}}{NA}, \qquad [1]$$

where $E_{Supercell}$ is the energy of the supercell containing the N equivalent planar defects, $E_{Perfect}$ is the energy of perfect w-BN with the same atoms as the supercell, N is the number of the planar defects, and A is the area of each planar defect. The formation energies of the (0001) ISF and {10$\bar{1}$0} IDB were calculated to be -0.331 J·m^{-2} and 0.313 J·m^{-2}, respectively. The formation energy of the (0001) ISF is negative because it has the same structure as c-BN, which is more stable than the w-BN phase.

1. R. F. Zhang, S. Veprek, A. S. Argon, Anisotropic ideal strengths and chemical bonding of wurtzite BN in comparison to zincblende BN. *Phys. Rev. B* **77**, 172103 (2008).
2. A. Nagakubo, H. Ogi, H. Sumiya, K. Kusakabe, M. Hirao, Elastic constants of cubic and wurtzite boron nitride. *Appl. Phys. Lett.* **102**, 241909 (2013).
3. M. Deura, K. Kutsukake, Y. Ohno, I. Yonenaga, T. Taniguchi, Nanoindentation measurements of a highly oriented wurtzite-type boron nitride bulk crystal. *Jpn. J. Appl. Phys.* **56**, 030301 (2017).
4. C. E. Dreyer, J. L. Lyons, A. Janotti, C. G. Van de Walle, Band alignments and polarization properties of BN polymorphs. *Appl. Phys. Express* **7**, 031001 (2014).
5. S. Yixi et al., Vacuum-ultraviolet reflectance spectra and optical properties of nanoscale wurtzite boron nitride. *Phys. Rev. B Condens. Matter* **50**, 18637–18639 (1994).
6. F. P. Bundy, F. P. Wentorf, Jr, Direct transformation of hexagonal boron nitride to denser forms. *J. Chem. Phys.* **38**, 1144–1149 (1963).
7. T. Soma, A. Sawaoka, S. Saito, Characterization of wurtzite type boron nitride synthesized by shock compression. *Mater. Res. Bull.* **9**, 755–762 (1974).
8. M. M. Bindal, B. P. Singh, S. K. Singhal, R. K. Nayar, R. Chopra, Sintering of wurtzitic boron nitride under high pressures and temperatures. *J. Mater. Sci. Lett.* **13**, 73–75 (1994).
9. C. Ji et al., Shear-induced phase transition of nanocrystalline hexagonal boron nitride to wurtzite structure at room temperature and lower pressure. *Proc. Natl. Acad. Sci. U.S.A.* **109**, 19108–19112 (2012).
10. G. S. Oleinik, Structural transformations in the formation of superhard materials based on the wurtzitic boron nitride initial powders. *J. Superhard Mater.* **34**, 1–18 (2012).
11. B. Vishal et al., Chemically stabilized epitaxial wurtzite-BN thin film. *Superlattices Microstruct.* **115**, 197–203 (2018).
12. Y. Meng et al., The formation of sp^3 bonding in compressed BN. *Nat. Mater.* **3**, 111–114 (2004).
13. Q. Johnson, A. C. Mitchell, First x-ray diffraction evidence for a phase transition during shock-wave compression. *Phys. Rev. Lett.* **29**, 1369–1371 (1972).
14. L. Hromadová, R. Martoňák, Pressure-induced structural transitions in BN from *ab initio* metadynamics. *Phys. Rev. B* **84**, 224108 (2011).
15. T. Taniguchi, T. Sato, W. Utsumi, T. Kikegawa, O. Shimomura, Effect of non-hydrostaticity on the pressure induced phase transformation of rhombohedral boron nitride. *Appl. Phys. Lett.* **70**, 2392–2394 (1997).
16. A. Onodera, H. Miyazaki, N. Fujimoto, Phase transformation of wurtzite-type boron nitride at high pressures and temperatures. *J. Chem. Phys.* **74**, 5814–5816 (1981).
17. Z. Pan, H. Sun, Y. Zhang, C. Chen, Harder than diamond: Superior indentation strength of wurtzite BN and lonsdaleite. *Phys. Rev. Lett.* **102**, 055503 (2009).
18. E. Tani, T. Soma, A. Sawaoka, S. Saito, A stability of wurtzite type boron nitride under high pressure. *Jpn. J. Appl. Phys.* **14**, 1605–1606 (1975).
19. T. Akashi, A. Sawaoka, S. Saito, Effect of TiB$_2$ and boron additions on the stability of wurtzite-type boron nitride at high temperatures and pressures. *J. Am. Ceram. Soc.* **61**, 245–246 (1978).
20. T. Akashi, A. Sawaoka, S. Saito, M. Araki, Structural changes of boron nitride caused by multiple shock-compressions. *Jpn. J. Appl. Phys.* **15**, 891–892 (1976).
21. T. Akashi, H. R. Pak, A. Sawaoka, Structural changes of wurtzite-type and zincblende-type boron nitrides by shock treatments. *J. Mater. Sci.* **21**, 4060–4066 (1986).
22. H. Yanagida, K. Koumoto, M. Miyayama, *The Chemistry of Ceramics* (John Wiley & Sons, 1996).
23. F. P. Bundy, J. S. Kasper, Hexagonal diamond—A new form of carbon. *J. Chem. Phys.* **46**, 3437–3446 (1967).
24. D. Kraus et al., Nanosecond formation of diamond and lonsdaleite by shock compression of graphite. *Nat. Commun.* **7**, 10970 (2016).
25. A. K. Jena, M. C. Chaturvedi, *Phase Transformation in Materials* (Prentice Hall, 1992).
26. T. Taniguchi, K. Watanabe, Synthesis of high-purity boron nitride single crystals under high pressure by using Ba-BN solvent. *J. Cryst. Growth* **303**, 525–529 (2007).
27. M. Chubarov, H. Högberg, A. Henry, H. Pedersen, Review article: Challenge in determining the crystal structure of epitaxial 0001 oriented sp(2)-BN. *J. Vac. Sci. Technol. A* **36**, 030801 (2018).
28. N. Ohba, K. Miwa, N. Nagasako, A. Fukumoto, First-principles study on structural, dielectric, and dynamical properties for three BN polytypes. *Phys. Rev. B* **63**, 115207 (2001). Correction in: *Phys. Rev. B.* **77**, 129901 (2008).
29. C. Chen et al., Misfit accommodation mechanism at the heterointerface between diamond and cubic boron nitride. *Nat. Commun.* **6**, 6327 (2015).
30. C. Iwamoto, S. Statonaka, T. Yamamoto, Y. Ikuhara, H. Matsuhata, 1Å-resolution chemical imaging by phase contrast technique. *J. Appl. Phys.* **99**, 104909 (2006).
31. C. Iwamoto, X. Q. Shen, H. Okumura, H. Matsuhata, Y. Ikuhara, Termination mechanism of inversion domains by stacking faults in GaN. *J. Appl. Phys.* **93**, 3264–3269 (2003).
32. S. J. Pennycook, L. A. Boatner, Chemically sensitive structure-imaging with a scanning transmission electron microscope. *Nature* **336**, 565–567 (1988).
33. S. D. Findlay et al., Robust atomic resolution imaging of light elements using scanning transmission electron microscopy. *Appl. Phys. Lett.* **95**, 191913 (2009).
34. K. Kioseoglou et al., Junction lines of inversion domain boundaries with stacking faults in GaN. *Phys. Rev. B* **70**, 115331 (2004).
35. H. Razavi-Khosroshahi, K. Edalati, M. Arita, Z. Horita, M. Fuji, Plastic strain and grain size effect on high-pressure phase transformations in nanostructured TiO$_2$ ceramics. *Scr. Mater.* **124**, 59–62 (2016).
36. V. Swamy et al., Size-dependent pressure-induced amorphization in nanoscale TiO2. *Phys. Rev. Lett.* **96**, 135702 (2006).
37. E. S. Grew, G. Hystad, R. M. Hazen, S. V. Krivovichev, L. A. Gorelova, How many boron minerals occur in Earth's upper crust? *Am. Mineral.* **102**, 1573–1587 (2017).
38. L. F. Dobrzhinetskaya et al., Qingsongite, natural cubic boron nitride: The first boron mineral from the Earth's mantle. *Am. Mineral.* **99**, 764–772 (2014).
39. E. J. Kirkland, *Advanced Computing in Electron Microscopy* (Pleum, 1998).
40. G. Kresse, J. Furthmüller, Efficient iterative schemes for ab initio total-energy calculations using a plane-wave basis set. *Phys. Rev. B Condens. Matter* **54**, 11169–11186 (1996).
41. G. Kresse, J. Furthmüller, Efficiency of ab-initio total energy calculations for metals and semiconductors using a plane-wave basis set. *Comput. Mater. Sci.* **6**, 15–50 (1996).
42. P. E. Blöchl, Projector augmented-wave method. *Phys. Rev. B Condens. Matter* **50**, 17953–17979 (1994).
43. J. P. Perdew et al., Atoms, molecules, solids, and surfaces: Applications of the generalized gradient approximation for exchange and correlation. *Phys. Rev. B Condens. Matter* **46**, 6671–6687 (1992).
44. H. J. Monkhorst, J. D. Pack, Special points for Brillouin-zone integrations. *Phys. Rev. B* **13**, 5188–5192 (1976).